Internal wave excitation by a vertically oscillating elliptical cylinder

B. R. Sutherland[a)]
Department of Mathematical Sciences, University of Alberta, Edmonton, Alberta T6G 2G1, Canada

P. F. Linden
Department of Mechanical and Aerospace Engineering, University of California-San Diego, La Jolla, California 92093

(Received 26 June 2001; accepted 26 October 2001)

Laboratory experiments are performed to measure the amplitude of internal waves generated by an elliptical cylinder oscillating vertically with different frequencies and amplitudes in a uniformly stratified fluid. The experimental results are compared with the theoretical predictions of Hurley and Keady (1997). Though in qualitatively good agreement with experiments, the theory underestimates the amplitude of low-frequency waves and overestimates the amplitude of high-frequency waves. The measured beam width is underestimated by theory, which neglects the dynamics of viscous boundary layers surrounding the cylinder. When the cylinder oscillates at a frequency less than half the buoyancy frequency, experiments reveal that two sets of waves beams are generated. The secondary set of waves have double the frequency of the primary waves and are excited due to nonlinear processes. © *2002 American Institute of Physics.* [DOI: 10.1063/1.1430438]

I. INTRODUCTION

Internal waves propagate horizontally and vertically through density stratified fluids. In the atmosphere and ocean the waves transport momentum and energy vertically and accelerate the flow at levels where they break.[1–4] Despite their non-negligible impact upon large-scale geophysical flows, the processes by which internal waves are generated, propagate, interact and break are not well understood beyond linear theory.

One of the most significant sources of internal waves in the atmosphere is topographic forcing:[5] As wind blows over a mountain range, the air is forced vertically and, under suitable conditions, may generate internal waves. Linear theory assumes the height of the hills is small compared with their horizontal extent. Often free-slip boundary conditions are assumed, meaning that boundary layers (whether turbulent or laminar) are taken to be negligibly thin (e.g., see Gill,[6] Sec. 6).

If the heights of the hills are a significant fraction of their horizontal extent, linear theory breaks down for two reasons: The amplitude of the generated waves is not negligibly small, and turbulence may cause boundary layers to thicken to non-negligible size.[7]

To examine the characteristics of strongly forced internal waves and their interaction with boundary layers, we have performed laboratory experiments of the generation of waves from a vertically oscillating elliptical cylinder in uniformly density stratified fluid. Although the experiments model a process quite different from that of uniform flow over topography, the experiments provide a useful starting point for analyzing interactions between internal waves and boundary layers. The relative effect of boundary layers is modified by changing the aspect ratio of major and minor axes of the ellipse as well as the amplitude of oscillation. The results are compared with a recently developed theory that predicts the structure of small amplitude waves generated by an oscillating ellipse in inviscid[8] and viscous[9] fluid with no-slip boundaries.

The experiments themselves are similar to the classic oscillating circular cylinder experiments of Mowbray and Rarity.[10] In those experiments, a standard schlieren visualization system was used to measure the spatial extent and phase of the waves, but wave amplitudes could not be measured. We employ a new ''synthetic schlieren'' technique that nonintrusively measures the amplitude of internal waves everywhere in space and time.[11] This technique has been used to measure the amplitude of waves generated from a circular cylinder oscillating vertically[12] and at an angle to the vertical.[13]

In agreement with linear theory,[10,14–16] the synthetic schlieren circular cylinder experiments showed internal waves emanate from the cylinder as four beams that form a ''St. Andrew's Cross'' pattern with the cylinder at the center of the cross. This pattern formed if the frequency of oscillation of the cylinder was less than the natural frequency of vertical oscillation of the fluid (the ''buoyancy frequency''). The measured amplitude of the waves agreed well with the viscous theory of Hurley and Keady.[9] Nonetheless, some discrepancies were observed:[12,13] The theory predicted the waves should have attenuated over a longer distance than was in fact observed; the observed width of the wave beam was ~10% larger than predicted by theory; and the amplitude of low-frequency waves was underpredicted. The reason for the discrepancies was that the theory did not account for the development of a viscous boundary layer that surrounded the cylinder: The layer effectively increased the cylinder size

a)Author to whom correspondence should be addressed. Electronic mail: bruce.sutherland@ualberta.ca

and weakened the coupling of waves with the source.

By examining the dynamics of an oscillating elliptical cylinder, the relative effects of horizontal and vertical scales as well as amplitude can be examined. Furthermore, nonlinear interactions between internal waves are more easily analyzed. In the study of a vertically oscillating circular cylinder,[12] it was found that, contrary to theoretical predictions, the superposition of upward and downward propagating wave beams did not destructively cancel perfectly at their midpoint. Instead the local wave field exhibited oscillatory motion at double the cylinder oscillation frequency. In experiments where low-frequency waves were generated, waves with double the frequency of the cylinder were found to emanate from the source region forming a second St. Andrew's Cross pattern superimposed on the primary cross. It was hypothesized that these secondary waves were created due to nonlinear interactions between the primary upward and downward propagating waves. Experiments with elliptical cylinders give stronger signals from the secondary wave, and so provides the means to examine the nonlinear-interaction hypothesis in quantitative detail.

In Sec. II, we summarize the development and results of the inviscid and viscous theories of wave generation by an oscillating elliptical cylinder. The experiments and the use of ''synthetic schlieren'' to visualize waves and measure their amplitudes is described in Sec. III. In Sec. IV we compare theory with experiments. Specifically, we analyze the beam structure and amplitude as a function of the ellipticity, amplitude, and oscillation frequency of the cylinder. We also analyze the amplitude-dependence of the secondary wave beams with forcing amplitude. Results are summarized in Sec. V.

II. THEORY

Approximate theoretical solutions have been derived for inviscid[8] and viscously attenuating[9] internal waves generated by oscillating elliptical cylinders. Summaries of relevant aspects of the theory have been provided for the special case of a vertically oscillating circular cylinder[12] and of a circular cylinder oscillating at an angle to the vertical.[13]

Below we review the theory as it is applied specifically to the case of a vertically oscillating elliptical cylinder with its two axes, of half-length a and b, aligned in the horizontal and vertical directions, respectively, as shown in Fig. 1(a). The notation we use is modified slightly from that originally employed by Hurley and Keady.[9]

We assume the cylinder is oscillating in a uniformly stratified fluid with (constant) buoyancy frequency, N. The fluid is assumed to be Boussinesq, meaning that density variations are negligible except for their effect upon buoyancy forces. Practically, this reflects the fact that in experiments the total density of stratified saline water increases by less than 10 percent from the top to the bottom of the tank. Under this approximation, $N^2=-(g/\rho_0)d\overline{\rho}/dz$, where g is the acceleration of gravity, ρ_0 ($\simeq 1.0$ g/cm^3 for water) is a characteristic value of density, and $\overline{\rho}(z)$ is the background density as a function of height, z.

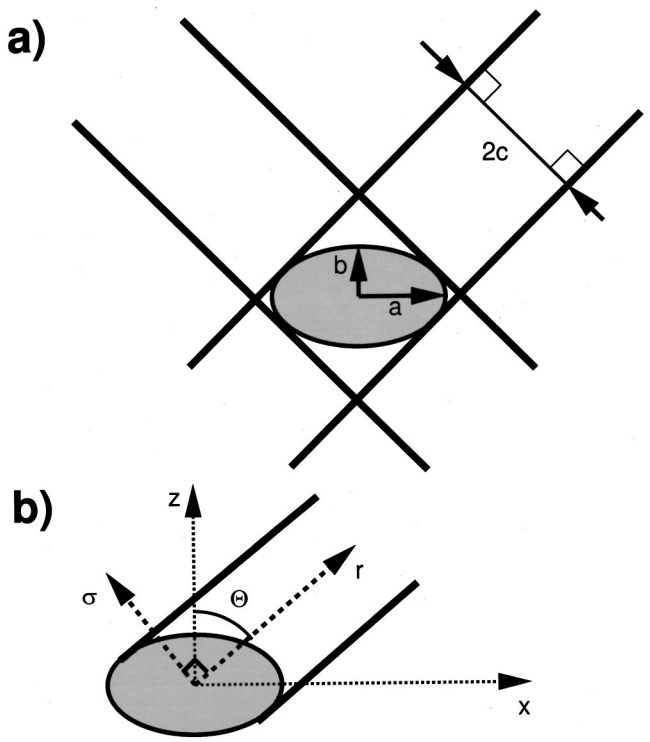

FIG. 1. (a) Geometry of the ellipse and the wave beams it generates. (b) Coordinate system used to model the right- and upward-propagating beam.

The amplitude of the cylinder (half the peak-to-peak vertical displacement) is denoted by A, and its (angular) frequency is denoted by ω. In all the experiments reported upon here, we set $\omega<N$, corresponding to the circumstance in which waves propagate away from the cylinder.

Assuming the wave structure is uniform along the length of the cylinder and assuming the fluid is incompressible, the wave motion is described by the streamfunction $\Psi(x,z,t)=\psi(x,z)\exp(-\imath\omega t)$, in which $\psi(x,z)$ is the streamfunction amplitude. Once ψ is determined, the horizontal (u) and vertical (w) components of the velocity field are given by

$$u=-\frac{\partial\psi}{\partial z}e^{-\imath\omega t}, \quad w=\frac{\partial\psi}{\partial x}e^{-\imath\omega t}.$$

For small amplitude waves, the Navier–Stokes and continuity equations may be simplified to give a single, fourth-order partial differential equation in ψ:

$$N^2\frac{\partial^2\psi}{\partial x^2}-\omega^2\nabla^2\psi+\imath\omega\nu\nabla^4\psi=0, \tag{1}$$

in which ν ($\simeq 0.01$ cm^2/s for water) is the kinematic viscosity.

If viscosity is neglected (i.e., $\nu=0$) and assuming $\omega<N$, the equation is simplified through a transformation, which amounts to re-writing the equations in a co-ordinate system with one axis, r, directed along the right and upward propagating beam and the other axis, σ, perpendicular to it, as shown in Fig. 1(b). Explicitly

$$\sigma=-x\cos\Theta+z\sin\Theta, \quad r=x\sin\Theta+z\cos\Theta.$$

Here $\Theta=\cos^{-1}(\omega/N)$ is the angle between the z- and r-axes (i.e., between the vertical axis and the wave beam). The solution of the resulting equation for the right and upward propagating wave beam is[8]

$$\psi(r,\sigma)=\frac{c\,\alpha}{-\sigma/c+(\sigma^2/c^2-1)^{(1/2)}}. \tag{2}$$

The structure of the other four beams may be found from (2) by symmetry. The result (2) involves the geometric constant, c, defined by

$$c^2=a^2\cos^2\Theta+b^2\sin^2\Theta, \tag{3}$$

and the amplitude-dependent constant

$$\alpha=\frac{1}{2}AN\frac{a^2}{c^2}\left[\frac{b}{a}\sin\Theta-\imath\cos\Theta\right]\cos\Theta. \tag{4}$$

Analysis of (2) reveals four qualitative features that are relevant here. First, the amplitude of the beam is constant in the along-beam direction. Variations along the beam occur only because of the superposition of the other two beams that cross it near the source. Second, the width of the wave beam is determined by c. For an elliptical cylinder, this is a function of the beam angle Θ. Indeed, a simple geometrical analysis shows[8] that $2c$ is the distance between the two parallel lines that are tangent to the ellipse and form an angle Θ to the vertical, as illustrated in Fig. 1(a). Third, there is a discontinuous phase change in the wave about $\sigma=\pm c$. Fourth, the along-beam velocity is infinite along the lines where $\sigma=c$.

The last two unphysical results are remedied by including the effects of viscosity. An explicit solution of (1) in (r,σ) co-ordinates is found by assuming that across-beam variations are more significant than along-beam variations (the boundary-layer approximation[14]). Thus, second- and fourth-order derivatives with respect to r are neglected and the equation becomes

$$-\frac{\partial^2\psi}{\partial\sigma\partial r}+\frac{\imath\nu}{2\omega\tan\Theta}\frac{\partial^4\psi}{\partial\sigma^4}=0. \tag{5}$$

Enforcing no-slip boundary conditions on the cylinder surface, the solution to (5), for $r>0$, is[9]

$$\psi=-\imath\alpha c\int_0^\infty\frac{J_1(k)}{k}\exp\left(-k^3\lambda\frac{r}{c}-\imath k\frac{\sigma}{c}\right)dk, \tag{6}$$

in which

$$\lambda=\frac{\nu}{2c^2N\sin\Theta}, \tag{7}$$

and J_1 is the first-order Bessel function of the first kind.

The result is used to find the amplitude of the vertical displacement field $\xi(x,z)$ given by

$$\xi=(\imath/\omega)\frac{\partial\psi(x,z)}{\partial x}\simeq(-\imath/\omega)\cos\Theta\frac{\partial\psi(r,\sigma)}{\partial\sigma},$$

where the boundary layer approximation has been used.

Figure 2 shows the predicted structure of up and rightward propagating waves generated by an oscillating elliptical cylinder. The calculated vertical displacement field is normalized by the vertical displacement A of the cylinder. The plots of amplitude at different phases, ϕ, of oscillation are shown in Figs. 2(a) and 2(b). As expected for waves with upward group velocity, the phase lines move downward (to decreasing σ) as ϕ increases. The amplitude of the envelope near the cylinder exhibits two peaks near $\sigma=\pm c$. Further from the cylinder, these peaks merge as the wave beam spreads due to viscosity. At $r=20$ cm, the peak amplitude occurs along the centerline of the beam (where $\sigma=0$).

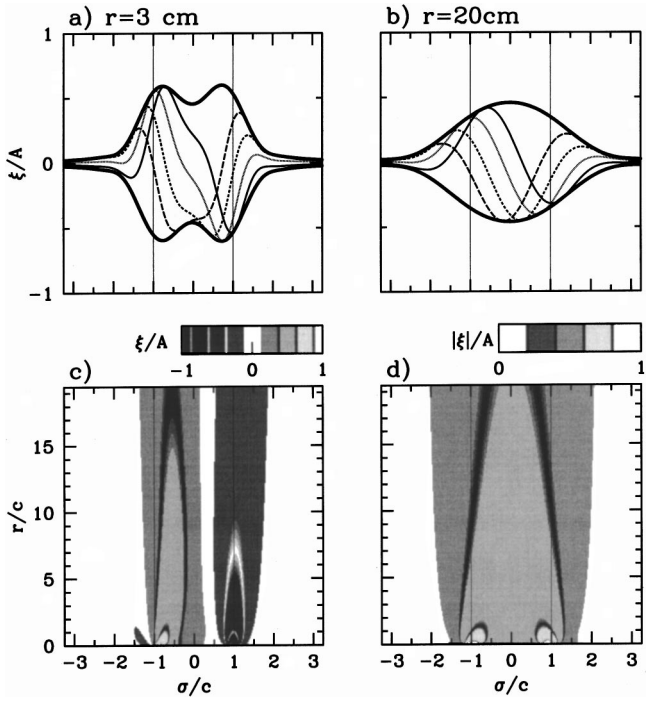

FIG. 2. Theoretical values of $\xi(r,\sigma)/A$ evaluated at along-beam distances (a) $r=3$ cm and (b) 20 cm for a cylinder with $\mu=3$ oscillating with relative frequency $\omega/N=0.54$. The plots show both the envelope (thick solid lines) and the instantaneous amplitude of the waves at phase $\phi=0$ (thin solid line), $\phi=\pi/4$ (dotted line), $\phi=\pi/2$ (short-dashed line), $\phi=3\pi/4$ (long-dashed line). The thin vertical lines in both plots illustrates the values $\sigma=\pm c$. Contours of ξ/A at phase $\phi=0$ are shown in (c), and (d) shows contours of the envelope of ξ/A.

The continuous change from the near-cylinder to far-cylinder structure is shown in Figs. 2(c) and 2(d), which illustrate the normalized amplitude of the wave beam using the gray-scale shown. Both diagrams show rapidly decreasing wave amplitudes near the cylinder about $\sigma=\pm c$. Farther from the cylinder the beam widens and the centerline amplitude decreases at a significantly slower rate.

For comparison with experiments, we find the amplitude of the time derivative of the perturbation squared buoyancy frequency: $N^2{}_t(x,z)$. Explicitly, using linear theory

$$N^2{}_t=-\imath\omega\left(-\frac{g}{\rho_0}\frac{\partial\rho}{\partial z}\right)\simeq N^2\cos\Theta\sin\Theta\frac{\partial^2\psi(r,\sigma)}{\partial\sigma^2}.$$

Hence

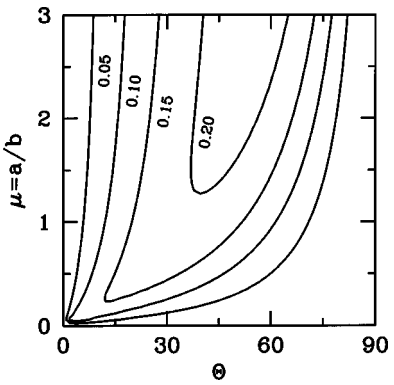

FIG. 3. The normalized amplitude $A_{N^2{}_t}/N^3(A/(a+b)/2)^{-1}$ for different Θ and $\mu=a/b$. Contours are shown by intervals of 0.05, as indicated.

$$N^2{}_t = N^2 \cos\Theta \sin\Theta \left(\frac{\imath\alpha}{c}\right) \int_0^\infty k J_1(k) \times \exp\left(-k^3\lambda \frac{r}{c} - \imath k \frac{\sigma}{c}\right) dk. \tag{8}$$

For fixed values of r, this integral is solved using a fast Fourier transform algorithm.[17]

In particular, along the centerline of the beam the magnitude of the $N^2{}_t$ field is given by

$$N^2{}_t|_{\sigma=0} = A_{N^2{}_t} \int_0^\infty J_1(k) k \exp(-k^3\lambda r/c) dk, \tag{9}$$

where

$$A_{N^2{}_t} = N^3 \cos^2\Theta \sin\Theta \left(\frac{a}{2c^2}\right) A, \tag{10}$$

is a characteristic measure of the wave beam's amplitude for $\sigma=0$ and $r\simeq 0$.

Figure 3 shows how $A_{N^2{}_t}$ depends upon the frequency and eccentricity of the cylinder. The diagram shows contours of the right-hand side of (10) after it is divided by the normalizing factors N^3 and the relative vertical displacement $A/[(a+b)/2]$. The frequency is given implicitly as a function of $\Theta=\cos^{-1}(\omega/N)$, and the eccentricity is given in terms of $\mu=a/b$. For fixed amplitude A and fixed $(a+b)/2$, the amplitude of the wave beam is larger if the cylinder is more eccentric. For μ fixed, the peak amplitude occurs for values of Θ between 0° and 90°, and this critical value of Θ increases as μ increases. This plot demonstrates why we observe a stronger signal from waves generated by oscillating elliptical cylinders with $\mu>1$.

The theoretical envelopes of the $N^2{}_t$ field in six cases are shown in Fig. 4. The diagrams show the superposition of the upward and downward propagating beams to the right of the cylinder. Note that the beams interfere destructively at $z=0$, so the amplitude of the superimposed beams is zero along the x axis.

The approximations leading to (5) are applicable for describing internal waves far from the source. Near the source, however, the amplitude of the internal waves is sufficiently large that linear theory does not necessarily apply. Even including viscous effects, the theory predicts unphysically large velocities close to the source, specifically for $|\sigma|\simeq c$ and $r \ll c/(\lambda(2\pi)^3)$. For experiments discussed here, this occurs if $r \ll 0.5c$, which is sufficiently large compared with the cylinder size that we expect the theory does not accurately model the coupling between waves and the cylinder.

In reality, a viscous boundary layer encompasses the cylinder as it oscillates and the approximation $\partial/\partial r \ll \partial/\partial\sigma$ breaks down for small r. For small-amplitude oscillations $(A \ll c)$ and neglecting the effects of density variations across the diameter of the cylinder, it can be shown that the boundary thickness is[18]

$$\delta \simeq \sqrt{2\nu/\omega}, \tag{11}$$

which is independent of the amplitude and size of the cylinder. For experiments discussed here, $0.1\ \mathrm{s}^{-1} \lesssim \omega \lesssim 0.6\ \mathrm{s}^{-1}$,

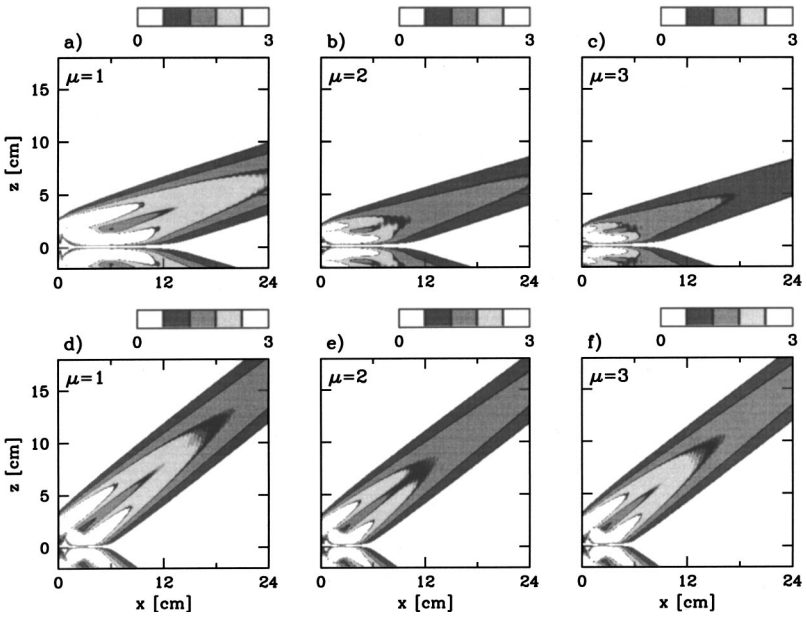

FIG. 4. Theoretical values of $\langle N^2{}_t\rangle/A_{N^2{}_t}$ evaluated for waves generated by an elliptical cylinder with (a) $\mu=1$, (b) 2, and (c) 3, and oscillating with relative frequency $\omega/N=0.26$. The corresponding fields are shown in (d)–(f) for the cylinder oscillating with relative frequency $\omega/N=0.55$.

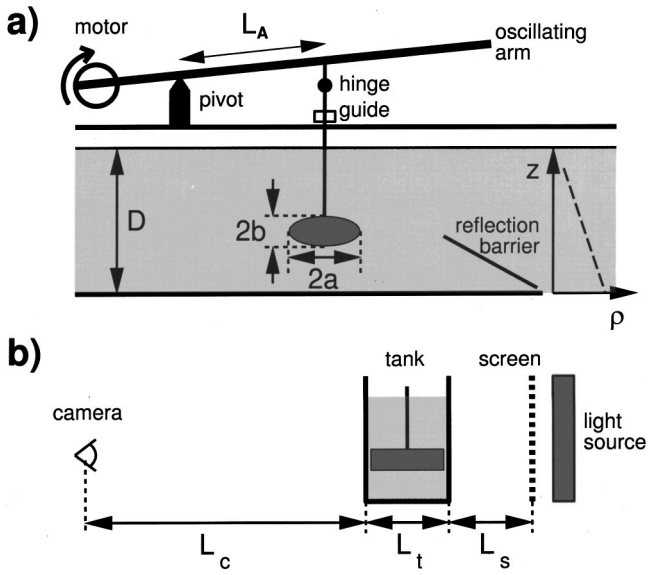

FIG. 5. (a) Front view of experimental set-up showing the oscillating cylinder mechanism. (b) Cross-sectional side view of the tank showing set-up for visualization of internal waves by synthetic schlieren.

and hence 0.4 cm$\gtrsim\delta\gtrsim$0.2 cm. Thus we expect the boundary layer to be a significant fraction of the cylinder size (see Sec. III) and as large as the amplitude of oscillation itself.

III. EXPERIMENTAL SET-UP

The experiments are performed in the test section of a long (over 200 cm) Perspex tank with width $L_t=20.0$ cm and height 50 cm. One of three 19.8 cm long cylinders is suspended in the tank with its axis spanning the tank width. The cross-section of each cylinder is elliptical with major and minor axes aligned in the horizontal and vertical directions, respectively. The eccentricity is characterized by the ratio $\mu=a/b$. If $a\geqslant b$, the eccentricity itself is $e=(1-\mu^{-2})^{(1/2)}$. Explicitly, the dimensions of the ellipses are $a=b=1.67$ cm ($\mu=1$, $e=0$: a circular cylinder); $a=2.19$ cm and $b=1.12$ cm ($\mu\simeq 2$, $e=0.86$); and $a=2.52$ cm and $b=0.86$ cm ($\mu\simeq 3$, $e=0.94$). In all three cases, the cylinder size is set so that the average $(a+b)/2$ is approximately the same. The cylinders are composed of PVC and the circular cylinder is hollow with removable ends which allow it to be filled partially with water in order to reduce its effective weight when suspended underwater.

Each cylinder is suspended from its center by a long thin metal rod, the other end of which is attached along a sinusoidally oscillating arm. To ensure purely vertical motion, the top of the rod is hinged and the rod itself is confined to pass between two guides, as shown in Fig. 5(a).

When attached at a position 45 cm along the arm (near its end) the cylinder undergoes a peak to peak displacement of $2A=0.64$ cm. The resulting flow surrounding the cylinders is laminar for all circumstances examined, although the fluid on either side of the cylinder with $\mu=3$ is on the verge of overturning when it oscillates at large amplitude.

The tank is filled with an approximately uniform stratified salt solution using a "double bucket" system.[19] In all cases the buoyancy frequency is set with $N\simeq 0.97\pm 0.05\ \mathrm{s}^{-1}$ over 32 cm depth. Each cylinder is suspended with its center 11.9 cm above the bottom of the tank. An angled barrier spanning the width of the tank is positioned sufficiently close to it to block upward propagating waves that reflect from the bottom. The barrier is not so close that it interferes with the waves generated near the cylinder.

A synthetic schlieren system[12] is used to visualize the internal waves. This technique is preferred over other schlieren and interferometric methods[11,20] because of its ability to measure very small wave amplitudes nonintrusively. In the set-up employed here, a translucent screen of evenly spaced 2 mm thick horizontal black lines is positioned $L_s=34.2$ cm behind the tank and is illuminated by fluorescent bulbs, as shown in Fig. 5(b).

A CCD camera is positioned $L_c=350$ cm from the front of the tank centered so that the elliptical cylinder is near the bottom left-hand side of the image and the screen of horizontal lines entirely fills the field of view. The signal from the camera is fed to a computer running the software package DIGIMAGE,[21] which digitizes, enhances and manipulates the images.

Synthetic schlieren, as with classical schlieren methods, works by monitoring how light is deflected as it passes through a stratified medium. If the fluid is strongly stratified, the light is deflected more than if it weakly stratified. Because internal waves stretch and compress constant density surfaces they locally change the stratification and, hence, the degree to which light is deflected. Synthetic schlieren thus measures the amplitude of the internal waves by measuring the distortion of the image of horizontal lines.

Synthetic schlieren directly measures changes in the density gradient, from which vertical displacement and velocity fields can be deduced. If Δz is the vertical displacement from its initial position of a point on the image of horizontal lines, then with our experimental set-up the corresponding local change in the buoyancy frequency is

$$\Delta N^2\simeq -(4.7\ \mathrm{s}^{-2}\,\mathrm{cm}^{-1})\Delta z. \tag{12}$$

The constant on the right-hand side is determined from L_t and L_s as well as physical constants including gravity, the indices of refraction of air and water, and the rate of change of index of refraction with salinity [see Sutherland *et al.*,[12] Eq. (2.11)].

Under ideal conditions, deflections as small as 0.001 cm can be detected so that changes of $\Delta N^2\gtrsim 0.005N^2$ can be measured. In practice, thermal variations in the laboratory and electronic noise make it necessary to filter and enhance the image.

A second directly measurable dynamical field is the time derivative of the ΔN^2 field, N^2_t. This is measured by determining the displacement Δz of the corresponding pixels in two images taken a short time Δt apart during an experiment. The N^2_t field is found by calculating ΔN^2 in (12) and dividing the result by Δt. Typically, we use $\Delta t\simeq 0.2$ s, a small fraction of the wave period.

An example of the use of synthetic schlieren is shown in Fig. 6. The unenhanced image taken by the CCD camera is shown in Fig. 6(a). This shows the side view of the elliptical

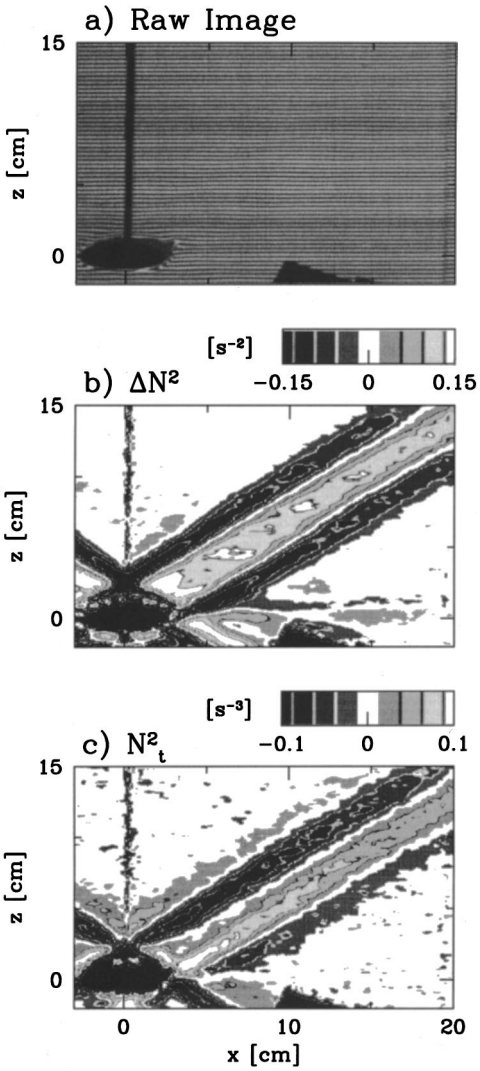

FIG. 6. (a) Snapshot of an elliptical cylinder with $\mu=3$ and the illuminated screen of horizontal lines behind the tank. The cylinder oscillates with relative frequency $\omega/N=0.54$, and the image is taken as it moves downward through the origin. The (b) ΔN^2 and (c) $N^2{}_t$ fields computed from the measured distortion of the image of lines due to internal waves.

cylinder (with $\mu=3$) centered at the origin. The vertical black line above the cylinder is the thin rod from which the cylinder is suspended. The end of the reflecting barrier 10 cm to the right of the cylinder can be seen. The image of lines behind the tank dominates the field of view. This image is taken during the course of an experiment in which the cylinder has been oscillating for many periods. As predicted, internal waves emanate from the cylinder along four beams. Indeed, close to the cylinder, distortions in the background image can be seen with the naked eye. Computer enhancement helps visualize the distortions further from the cylinder and measurements of the ΔN^2 and $N^2{}_t$ fields can be made, as shown in Figs. 6(b) and 6(c), respectively.

Both fields show the up- and rightward-propagating wave beam. Consistent with linear theory,[13] the $N^2{}_t$ field is 90° out of phase with the ΔN^2 field.

The ΔN^2 field generally gives a stronger signal. However, it is contaminated by slowly evolving density variations in the tank evident as the horizontal gray bands near $z=0$ in Fig. 6(b). This occurs due to diffusive mixing which is inevitable in a stratified fluid near the sloping boundaries of the cylinder.[22,23] The signal from the ΔN^2 field is further contaminated by the slowly evolving temperature variations in the laboratory.

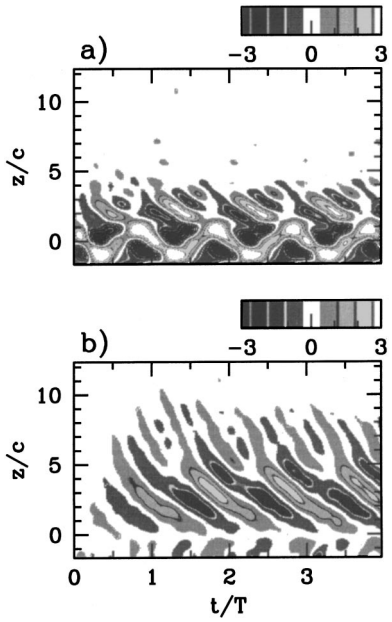

FIG. 7. Time series, $N^2{}_t(z,t;x_0)/A_{N^2{}_t}$, for an elliptical cylinder with $\mu=2$, oscillating with relative frequency $\omega/N=0.25$ and amplitude $A=0.32$ cm. The time series are taken at horizontal positions (a) $x=2.5$ cm $(2.1c)$ and (b) 12.5 cm $(10.3c)$ from the center of the cylinder. Time is normalized by the forcing period $T=2\pi/\omega$.

For this reason, the $N^2{}_t$ field is analyzed in detail here: Taking the time-derivative of the ΔN^2 field effectively filters slowly evolving processes. This analysis is described in the next section.

IV. RESULTS

Theory agrees qualitatively with the experimental results shown in plots like those in Figs. 6(b) and 6(c). Four wave beams emanate from the oscillating cylinder each oriented at a fixed angle from the vertical. Energy is transported radially along the beams while phase lines propagate across the beams. In particular, for the right- and upward-propagating wave beam, the phase lines move downward over time.

Using synthetic schlieren, the amplitude of the waves may also be compared directly with theoretical predictions.

A. Time-series analysis

The temporal behavior of the wave beams is analyzed using time series images of the experiments. For example, Fig. 7 shows two time series determined from an experiment in which a cylinder with $\mu=2$ oscillates at frequency $\omega=0.25\ \mathrm{s}^{-1}$ (period $T=25.1$ s). In both the cylinder starts oscillating at time $t=0$. Figure 7(a) shows the evolution over 99.6 seconds of the $N^2{}_t$ field along a vertical cross section taken 2.5 cm to the right of the cylinder. At this proximity, the upward- and downward-propagating wave beams overlap. The field varies periodically with dominant period equal

to that of the oscillating cylinder. However, whereas theory predicts perfect destructive interference between the two wave beams, the experiment shows that $N^2{}_t$ is not exactly zero where $z=0$. Instead the field varies between positive and negative values with frequency double that of the cylinder's oscillation.

Figure 7(b) shows the evolution of the $N^2{}_t$ field along a vertical cross section taken 12.5 cm to the right of the cylinder. The field grows to non-negligible values a short time after the cylinder begins to oscillate, consistent with the time for energy to propagate at the horizontal group velocity from the cylinder to this position. Afterwards the field evolves in steady state, oscillating between positive and negative values. At this distance from the cylinder, the upward propagating beam does not interfere significantly with the downward propagating beam. The peak amplitudes occur for $1 \lesssim z \lesssim 5$, consistent with the range expected for the upward propagating beam. For $5 \lesssim z \lesssim 12$, the $N^2{}_t$ field oscillates with double the frequency of oscillation of the cylinder. In Fig. 7(a) (at $x=2.5$), the frequency-doubled signal is apparent for $3 \lesssim z \lesssim 5$. In Sec. IV D it will be shown that this results from a secondary wave beam generated as a result of wave–wave interactions in the overlap region.

To compare the $N^2{}_t$ field directly with theory, time-averaged signals are constructed from time series, such as those shown in Fig. 7. Specifically, time series of the $N^2{}_t$ field are taken simultaneously over an integer number of oscillation periods. There are 24 time series in all taken at horizontal positions $x=0.5$, 1.5, ..., 23.5 cm, with respect to the cylinder which is centered at the origin $(x=0)$. The phase and amplitude of the oscillating cylinder itself is determined from the time series at $x=0.5$ cm. Fourier analysis of the vertical position of the cylinder confirms that the motion is purely sinusoidal. The root-mean-square average is computed from the $N^2{}_t$ field of each time series, and the result is multiplied by $2^{1/2}$. Finally, the envelope of the $N^2{}_t$ field along the length of the wave beam is reconstructed by splicing together the 24 profiles of the $N^2{}_t$ root-mean-square amplitude. This averaging procedure helps reduce random signal noise while enhancing the persistent signal from the steadily oscillating wave beam.

Figure 8 shows the envelopes of the $N^2{}_t$ field determined from experiments of a cylinder with $\mu=3$ oscillating with four different frequencies. The field is normalized by $A_{N^2{}_t}$, given by (10). At low forcing frequencies [e.g., Fig. 8(a)], the upward-propagating beam is close to the horizontal and overlaps with the downward propagating beam over a long distance. At faster frequencies [e.g., Fig. 8(d)], the upward-propagating beam is more vertical.

In all four experiments the angle to the vertical of the wave beam is close to $\Theta=\cos^{-1}(\omega/N)$, as predicted by theory. This is illustrated by the plots of $z=x\cot(\Theta)$ superimposed on the $N^2{}_t$ field in each diagram of Fig. 8. The diagonal lines follow the centerline of the beam in each case.

B. Along-beam amplitude

Consistent with theory, the amplitude of the wave beam is larger if the forcing frequency is faster. However, whereas

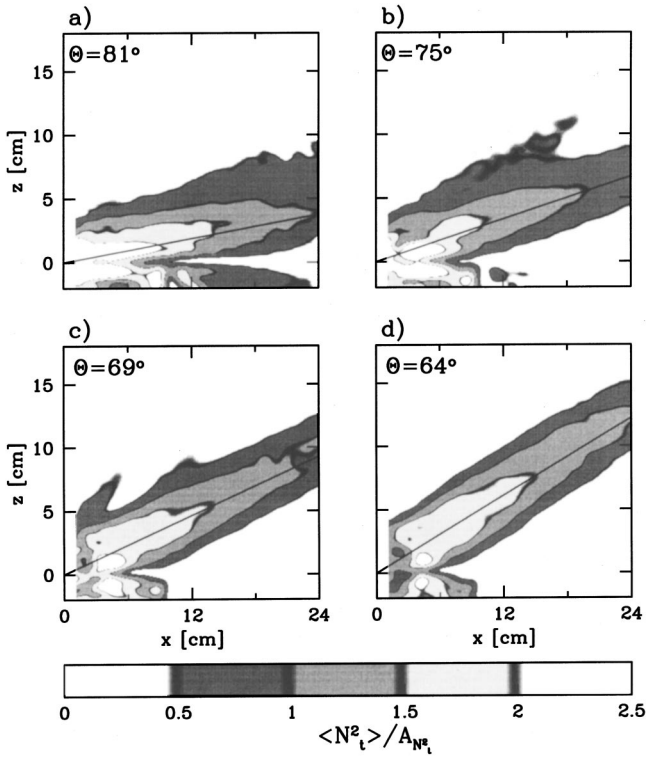

FIG. 8. Contours of $\langle N^2{}_t\rangle/A_{N^2{}_t}$ determined from four experiments of an elliptical cylinder with $\mu=3$, oscillating with amplitude $A=0.32$ cm at relative frequencies (a) $\omega/N=0.15$, (b) 0.26, (c) 0.35, and (d) 0.44. The corresponding values of $\Theta=\cos^{-1}(\omega/N)$ are indicated. Superimposed are plots of $z=x\cot\Theta$ (diagonal solid lines).

near the cylinder the theoretical amplitude envelopes, such as those shown in Fig. 4, are predicted to be largest on either flank of the beam's centerline, the experiment shows that the amplitude of the wave beams is in fact largest along the centerline only a short distance from the cylinder (e.g., see Fig. 8).

Figure 9 compares the amplitude of the normalized $N^2{}_t$ field along the centerline of the beam determined from four experiments. Figure 9(a) shows the amplitude functions, which are determined from cross sections of the $N^2{}_t$ field along the solid lines shown in each of the four fields shown in Fig. 8. The plots are shown for $3 \lesssim r \lesssim 24$ cm. The peaks for small r (i.e., $3 \lesssim r \lesssim 10$), occur in part due to the superposition of upward and downward propagating waves. For larger r the curves are representative of the centerline amplitude of a single beam.

The rescaled plots are shown in Fig. 9(b). To account for viscous attenuation, the along-beam distance, r, is thus rescaled by λ/c where c and λ are given by (3) and (7), respectively. Theory predicts that under this rescaling the five experimentally determined curves should collapse onto the theoretical curve (solid line), which is given by the integral in (9). When plotted on log–log axes, the curves for large ω/N are close to the theoretical prediction. However, the theory significantly underpredicts the amplitude of waves generated with low-frequency forcing.

The curves appear to exhibit power law scaling for $d=\lambda r/c \gtrsim 0.05$. The best fit line to $\ln(N^2{}_t|_{\sigma=0})$ versus $\ln(d)$ for

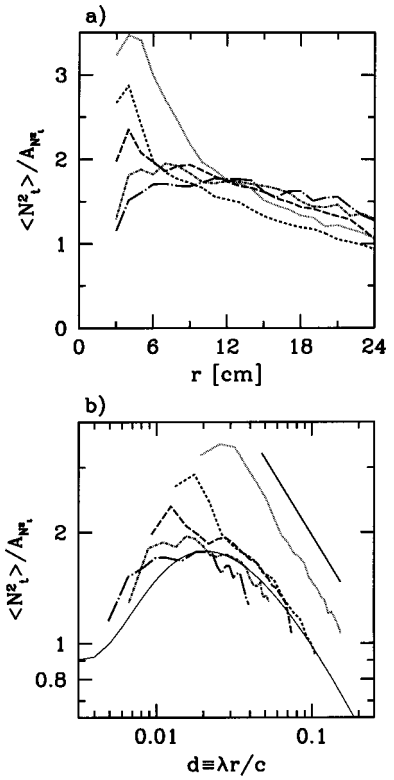

FIG. 9. (a) Normalized amplitude $\langle N^2{}_t\rangle/A_{N^2{}_t}$ versus radial distance r from the center of an oscillating elliptical cylinder with $\mu=3$, oscillating with amplitude $A=0.32$ cm at relative frequencies $\omega/N=0.15$ (dotted line), 0.26 (short-dashed line), 0.35 (long-dashed line), 0.44 (short-dash–dotted line), and 0.53 (long-dash–dotted line). In (b) the respective data are shown on a log–log plot with r scaled by λ/c. The thin solid curve shows the predicted amplitude. The diagonal solid line is the (vertically offset) best fit line to the experimental data with $\omega/N=0.15$ (dotted line).

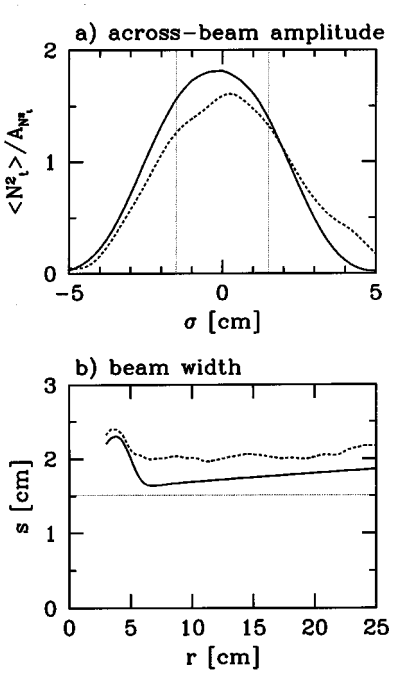

FIG. 10. Comparison between theory (solid line) and experiment (dashed line) of (a) across-beam amplitude at $r=20$ cm as a function of σ, and (b) beam width as a function of along-beam distance r, for a cylinder with $\mu=2$ oscillating with relative frequency $\omega/N=0.55$ and amplitude $A=0.32$ cm.

$7\leqslant r\leqslant 24$ cm has been determined for the slow frequency oscillation experiment with $\omega/N=0.15$. This (light solid) line is shown vertically offset from the corresponding raw data (dotted line) in Fig. 9(b). Its slope is -0.69 ± 0.04.

As shown in the Appendix, theory predicts that as $d\to\infty$, $N^2{}_t|_{\sigma=0}\propto d^{-1}$. This exponenent is less than the measured slope and is an indication that the experimentally generated wave beam in the field of view is not yet in the asymptotic regime where $d\gg 1$.

C. Across-beam amplitude and structure

The experimentally measured across-beam amplitude is compared with theory in Fig. 10. The theoretical amplitude-envelope of the beam far from the cylinder moderately overpredicts the observed amplitude.

The beam width, s, is measured by the standard deviation of the amplitude-envelope. The experimentally determined width as a function of along-beam distance r is compared with theory in Fig. 10(b). The graph shows that the theoretical beam width consistently underestimates the observed width even quite far from the cylinder. Whereas theory predicts an increase in the beam width with r, this behavior is not as evident in the experimental data over the range of r shown.

In experiments with low-frequency waves, the discrepancy is attributed, in part, to the presence of a superimposed secondary set of wave beams with double the frequency of the primary waves. The superimposed waves effectively broaden the width of the upper flank of the primary wave

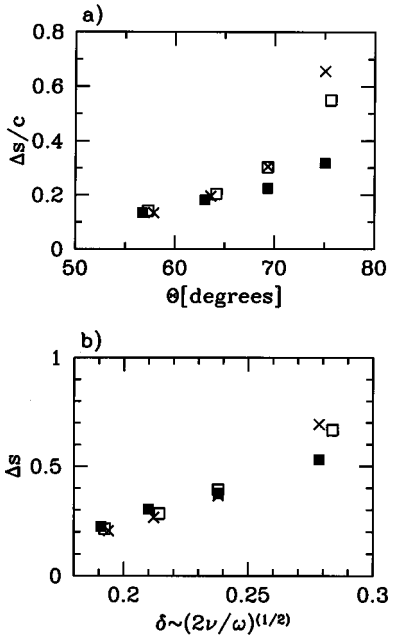

FIG. 11. (a) Relative difference $\Delta s/c$ between experimental and theoretical beam widths as a function of $\Theta=\cos^{-1}(\omega/N)$ and cylinder eccentricity corresponding to $\mu=1$ (solid square), $\mu=2$ (open square), and $\mu=3$ (cross). Errors in $\Delta s/c$ are ±0.1. For the same experiments, (b) plots the Δs versus the predicted boundary layer thickness, δ. The amplitude of oscillation is $A=0.32$ cm in all cases.

beam. However, in experiments with high-frequency waves (as Fig. 10), no secondary wave beams occur and, nonetheless, the beam width is underpredicted.

Figure 11 further quantifies the dependence of beam width upon experimental parameters. Figure 11(a) plots the normalized difference in beam width, $\Delta s/c$, versus Θ, where Δs is the average difference between the experimental and theoretical beam width (the standard deviations) measured for $18 \leqslant r \leqslant 20$ cm. The vertical error bars associated with each point extend between $\pm 10\%$ of $\Delta s/c$. In all experiments, the discrepancy increases with increasing Θ and hence with decreasing $\omega = N \cos\Theta$. In the case $\Theta \simeq 75°$, the discrepancy is attributed, in part, to the superposition of the secondary wave beams. Because the signal from the secondary wave beams is strongest in experiments with more eccentric cylinders, the discrepancy increases as μ increases.

In experiments with higher-frequency waves, the amplitude of the secondary waves, if they occur at all, is negligibly small near the primary beam for $18 \leqslant r \leqslant 20$ cm [e.g., see Figs. 8(c) and 8(d)]. Thus, other dynamics are responsible for the discrepancy. Indeed, it seems reasonable to attribute the discrepancy to viscous boundary layers, which are neglected in theory.

To examine this hypothesis, the rescaled data are plotted in Fig. 11(b), which shows values of Δs versus the predicted boundary layer width δ given by (11). The plot shows an approximately linear relationship between Δs and δ. Indeed, for the experiment with $\mu = 1$, the best fit line through the data (plotted by the four solid squares) gives $\Delta s \simeq 3.85\ (\pm 0.03)\,\delta - 0.5(\pm 0.1)$.

The line's intercept is sufficiently different than zero, that the anticipated dependence $\Delta s \propto \delta$ is brought into question. Indeed, the best fit line through a plot of $\log(\Delta\sigma)$ *versus* $\log(\omega)$ gives $\Delta\sigma \propto \omega^{-1.1(\pm 0.2)}$.

Why the exponent differs significantly from $-1/2$ is unclear, though not unexpected. The scaling theory assumptions leading to (11) are valid only in the limit $|\underline{u} \cdot \nabla \underline{u}|/|\partial \underline{u}/\partial t| \sim O(A/R) \ll 1$. However, the oscillation amplitude $A = 0.32$ is as large as 20% of the characteristic cylinder size, $R = (a+b)/2$. Indeed, if the amplitude $A = 0.32$, it is comparable with the boundary layer thickness δ.

D. Frequency-doubled waves

In experiments with a slowly oscillating cylinder, in addition to the dominant pattern of four wave beams, a second set of four wave beams are also observed. Time series of the waves, such as those shown in Fig. 7 reveal that the secondary waves have double the frequency of the primary waves, and hence double the frequency of oscillation of the cylinder itself.

The waves are generated due to nonlinear effects, as demonstrated by Fig. 12. This shows the envelope of the right- and upward-propagating wave beams in four experiments of a cylinder with $\mu = 2$ oscillating at different amplitudes but with the same frequency. Each diagram shows the $N^2{}_t$ field normalized by the amplitude $A_{N^2{}_t}$, which is proportional to the amplitude, A, of oscillation of the cylinder.

Superimposed on all four diagrams is a solid line which

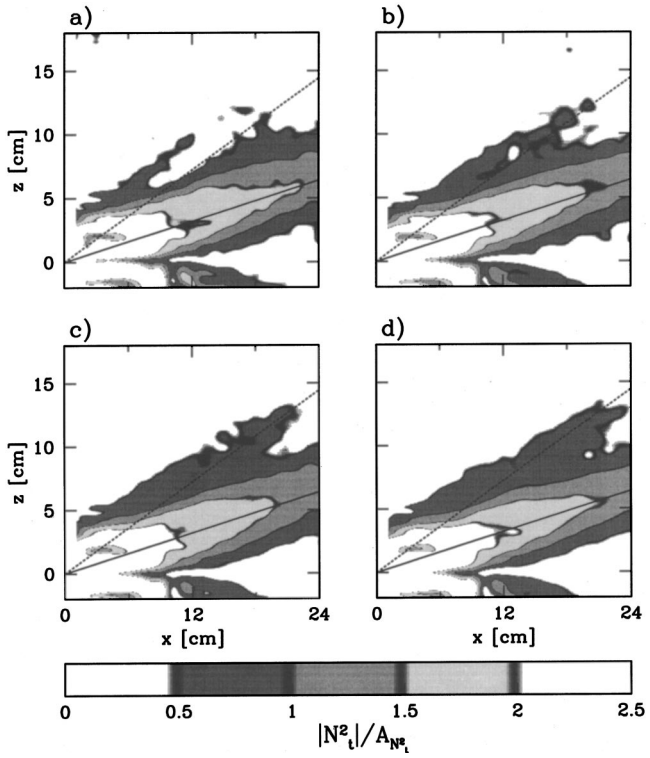

FIG. 12. Contours of the normalized envelope of the $N^2{}_t$ field for four experiments of an elliptical cylinder with $\mu \simeq 2$, oscillating at relative frequency $\omega/N \simeq 0.25$ with amplitude (a) $A = 0.18$, (b) 0.21, (c) 0.25, and (d) 0.28 cm.

forms an angle Θ to the vertical, where $\Theta = \cos^{-1}(\omega/N) \simeq 76°$. The line passes along the center of the primary wave beams in all four experiments. Also superimposed on each diagram of Fig. 12 is a dashed line which forms an angle Θ_2 to the vertical, where $\Theta_2 = \cos^{-1}(2\omega/N) \simeq 60°$. This line passes through the center of the secondary wave beam, consistent with the observation that the beam is composed of waves with double the cylinder oscillation frequency.

In all four experiments, the primary wave beam has approximately the same structure and normalized amplitude. However, the amplitude of the secondary wave beam is evidently not proportional to A, but increases faster than A. This nonlinear amplitude dependence is examined in more detail in Fig. 13, which shows the amplitude of the $N^2{}_t$ field along the centerline of the primary and secondary wave beams in the four experiments shown in Fig. 12, as well as a fifth corresponding experiment in which the amplitude of oscillation of the cylinder is $A = 0.32$ cm.

The results from the five experiments are shown collectively in Fig. 13. The five curves with larger amplitudes are taken along the center of the primary wave beam (e.g., the solid lines in Fig. 12). These amplitude-dependent functions, after normalization by $A_{N^2{}_t}$, collapse approximately onto a single curve.

The five curves with smaller amplitudes in Fig. 13(a) are taken along the center of the secondary wave beam (e.g., along the dashed lines in Fig. 12). Although similar in form, the curves corresponding to experiments with smaller forc-

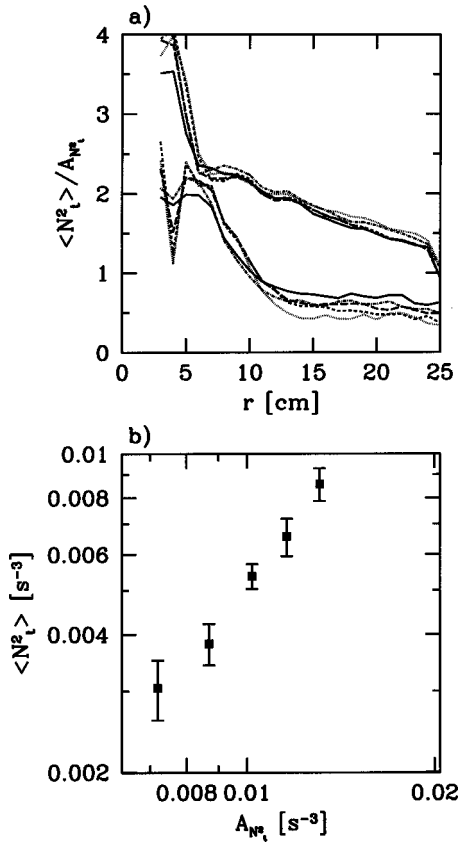

FIG. 13. (a) Normalized amplitude $\langle N^2{}_t\rangle/A_{N^2{}_t}$ versus radial distance r from the center of an elliptical cylinder, with $\mu=2$, oscillating with relative frequency $\omega/N=0.25$ and with amplitude $A=0.178$ (dotted line), 0.213 (short-dashed line), 0.249 (long-dashed line), 0.284 (dash–dotted line), and 0.320 (solid line). Amplitudes are determined along the two rays shown in Fig. 12. The log–log plot in (b) shows the corresponding unnormalized amplitudes averaged over $20\leqslant r\leqslant 25$ cm and plotted versus $A_{N^2{}_t}$.

ing, generally have smaller amplitude, even after normalization by $A_{N^2{}_t}$.

To examine the dependence of secondary wave amplitudes upon forcing amplitude, the average value of $N^2{}_t$ is computed for $20\leqslant r\leqslant 25$ cm for each of the five secondary wave beam amplitudes. The resulting five points are plotted versus $A_{N^2{}_t}$ on a log–log graph in Fig. 13(b). The error bars indicate the standard deviation of the averaged data.

Computing the best fit line through the five points, we find that $\langle N^2{}_t\rangle\propto(A_{N^2{}_t})^{(1.8\pm0.5)}$. This power law exponent is consistent with the expected value of 2 that would arise, for example, from nonlinear wave–wave interactions between the upward and downward propagating primary wave beams.

Indeed, there is evidence for nonlinear interactions between these two wave beams in the overlap region near the cylinder. As shown in Fig. 7(a), along the x axis, the $N^2{}_t$ field varies with double the frequency of oscillation of the cylinder. This occurs contrary to linear theory, which predicts perfect destructive interference.

Other than wave–wave interactions, another nonlinear mechanism presents itself: the source of the secondary wave beams may be due to interactions between the primary wave beam and the (oscillating) viscous boundary layer surrounding the cylinder. In support of this hypothesis, we note that the secondary beams appear to radiate along rays emanating from the cylinder and not from the overlap region. Furthermore, the amplitude of the secondary beams near the cylinder appears peaked on either side of the centerline of the beam [e.g., see Figs. 12(a) and 12(b)]. This structure is similar to that of the primary beams near the cylinder. Finally, in fully nonlinear numerical simulations of large amplitude internal waves excited by an oscillating elliptical patch of fluid, secondary wave beams are not generated. It is believed this is because viscous boundary layers are absent in the simulations.

These observations motivate a theoretical and numerical investigation of internal waves generated by a solid oscillating cylinder that include the development of viscous boundary layers. Such research, however, is beyond the scope of the present work.

V. CONCLUSIONS

Using time series analyses of synthetic schlieren images, we have made accurate measurements of the envelope of internal wave beams generated by a vertically oscillating elliptical cylinder and we have compared the results with existing theoretical predictions. The theory includes viscous attenuation effects but ignores viscous boundary layers surrounding the cylinder and ignores large-amplitude effects.

The experiments show that theory underpredicts the amplitude of low-frequency waves and overpredicts the amplitude of high-frequency waves. In all cases the beam width is underpredicted, and the discrepancy increases with increasing boundary layer thickness. Finally, the appearance of secondary wave beams with double the frequency of oscillation of the cylinder have conclusively been shown to result from large-amplitude effects. Observations and negative results from fully nonlinear simulations that neglect boundary layers imply that the nonlinear dynamics involve interactions between waves and boundary layers. However, more research is necessary to test this hypothesis.

APPENDIX: ASYMPTOTIC ANALYSIS

Here the far-field power law behavior of the wave beam's amplitude along its centerline is diagnosed.

From (6), the streamfunction along the centerline of the right- and upward-propagating wave beam is

$$\psi|_{\sigma=0}\propto\int_0^\infty \frac{J_1(k)}{k}\exp(-k^3d)\ dk, \tag{A1}$$

where $d=\lambda\, r/c$.

Through differentiation of (6) with respect to σ, the asymptotic behavior of dynamical fields of interest can be deduced. For convenience, we define

$$f(d;p)=\int_0^\infty J_1(k)k^{p-1}\exp(-k^3d)\ dk. \tag{A2}$$

Then, for large d, the along-beam velocity is proportional to $f(d,1)$ and $N^2{}_t|_{\sigma=0}\propto f(d,2)$.

Standard asymptotic analyses (i.e., Watson's Lemma[24]) give, for $p>-1$,

$$f(d;p)\sim\frac{1}{6}d^{-(p+1)/3}\sum_{n=0}^{\infty}\frac{(-1)^n\Gamma\left(\frac{p+1+2n}{3}\right)}{2^{2n}n!(n+1)!}d^{-2n/3}. \tag{A3}$$

To leading order the far field along-beam velocity is predicted to decrease as $d^{-2/3}$, consistent with the prediction of Hurley and Keady.[9] The ${N^2}_t$ field is predicted to decrease as d^{-1}.

[1]C. O. Hines, "Internal atmospheric gravity waves at ionspheric heights," Can. J. Chem. **38**, 1441 (1960).
[2]R. S. Lindzen, "Turbulence and stress owing to gravity wave and tidal breakdown," J. Geophys. Res., [Oceans] **86**, 9707 (1981).
[3]N. A. McFarlane, "The effect of orographically excited gravity wave drag on the general circulation of the lower stratosphere and troposphere," J. Atmos. Sci. **44**, 1775 (1987).
[4]T. N. Palmer, G. J. Shutts, and R. Swinbank, "Alleviation of a systematic westerly bias in general circulation and numerical weather prediction models through an orographic gravity drag parametrization," Q. J. R. Meteorol. Soc. **112**, 1001 (1986).
[5]D. C. Fritts and G. D. Nastrom, "Sources of mesoscale variability of gravity waves. Part II: Frontal, convective, and jet stream excitation," J. Atmos. Sci. **49**, 111 (1992).
[6]A. E. Gill, *Atmosphere-Ocean Dynamics* (Academic, San Diego, 1982).
[7]P. G. Baines and K. P. Hoinka, "Stratified flow over two-dimensional topography in fluid of infinite depth: a laboratory simulation," J. Atmos. Sci. **42**, 1614 (1985).
[8]D. G. Hurley, "The generation of internal waves by vibrating elliptic cylinders. Part 1: Inviscid solution," J. Fluid Mech. **351**, 105 (1997).
[9]D. G. Hurley and G. Keady, "The generation of internal waves by vibrating elliptic cylinders. Part 2: Approximate viscous solution," J. Fluid Mech. **351**, 119 (1997).
[10]D. E. Mowbray and B. S. H. Rarity, "A theoretical and experimental investigation of the phase configuration of internal waves of small amplitude in a density stratified liquid," J. Fluid Mech. **28**, 1 (1967).
[11]S. B. Dalziel, G. O. Hughes, and B. R. Sutherland, "Whole field density measurements," Exp. Fluids **28**, 322 (2000).
[12]B. R. Sutherland, S. B. Dalziel, G. O. Hughes, and P. F. Linden, "Visualisation and measurement of internal waves by 'synthetic schlieren.' Part 1: Vertically oscillating cylinder," J. Fluid Mech. **390**, 93 (1999).
[13]B. R. Sutherland, G. O. Hughes, S. B. Dalziel, and P. F. Linden, "Internal waves revisited," Dyn. Atmos. Oceans **31**, 209 (2000).
[14]N. H. Thomas and T. N. Stevenson, "A similarity solution for viscous internal waves," J. Fluid Mech. **54**, 495 (1972).
[15]M. J. Lighthill, *Waves in Fluids* (Cambridge University Press, Cambridge, England, 1978).
[16]B. Voisin, "Internal wave generation in uniformly stratified fluids. Part 1. Green's function and point sources," J. Fluid Mech. **231**, 439 (1991).
[17]W. H. Press, B. P. Flannery, S. A. Teukolsky, and W. T. Vetterling, *Numerical Recipes: The Art of Scientific Computing*, 2nd ed. (Cambridge University Press, New York, 1993).
[18]G. K. Batchelor, *An Introduction to Fluid Dynamics* (Cambridge University Press, Cambridge, England, 1967).
[19]G. Oster, "Density gradients," Sci. Am. **213**, 70 (1965).
[20]W. Merzkirch, *Flow Visualization* (Academic, New York, 1974).
[21]S. B. Dalziel, "Decay of rotating turbulence: Some particle tracking experiments," Appl. Sci. Res. **49**, 217 (1992).
[22]O. M. Phillips, "On flows induced by diffusion in a stably stratified fluid," Deep-Sea Res. **17**, 435 (1970).
[23]C. Wunsch, "On oceanic boundary mixing," Deep-Sea Res. **17**, 293 (1970).
[24]C. M. Bender and S. A. Orszag, *Advanced Mathematical Methods for Scientists and Engineers* (Springer-Verlag, New York, 1999).